ACS APPLIED MATERIALS & INTERFACES

Research Article

www.acsami.org

Synthesis of Porous Hierarchical MgO and Its Superb Adsorption Properties

Peng Tian, Xiu-ying Han, Gui-ling Ning,* Hai-xia Fang, Jun-wei Ye, Wei-tao Gong, and Yuan Lin

State Key Laboratory of Fine Chemicals, School of Chemical Engineering, Dalian University of Technology, Dalian 116024, China

Supporting Information

ABSTRACT: The porous hierarchical MgO with superb adsorption properties has been synthesized by a facile and scaled-up method. The X-ray powder diffraction, electron microscopy, Fourier transformed infrared, and N_2 adsorption−desorption were carried out to study the microstructure of the as-synthesized precursor and product. It has been demonstrated that the as-prepared MgO has a porous hierarchical structure and a high specific surface area (148 m^2 g^{-1}). And the MgO sample exhibited super adsorption properties, with maximum adsorption capacity of 2409 mg g^{-1} for Congo red, which is the highest reported value. Moreover, the adsorption process of Congo red on porous hierarchical MgO was systematically investigated, which was found to obey the pseudo-second-order rate equation and Langmuir adsorption model.

KEYWORDS: *porous hierarchical structure, magnesium oxide, Congo red, adsorption*

1. INTRODUCTION

Dye is recognized to be the first contaminant in wastewater.[1,2] How to rationally and efficiently deal with dye-contaminated effluents before discharge is of great importance. Though a number of processes are available for dye removal from aqueous systems, adsorption is the most convenient and popular method because of its simplicity, high efficiency, and low energy requirements.[3−7] Nevertheless, the common adsorbents often only have limited adsorption capacities and low adsorption rates.[8] In recent years, porous hierarchically structured metal oxides and metal hydroxides were used for wastewater treatment and exhibited excellent adsorption performance.[8−15] Their micrometer-sized overall structure favors them to separate from water, and the porous hierarchical structure can provide a high specific surface area and a large surface-to-volume ratio for contact, plenty active sites for stay, and hierarchical channels for mass transfer.

As a nontoxic, economical, and environmentally friendly material, MgO has already been widely used to treat wastewater.[16−21] Recently, several highlighted works reported the synthesis of porous hierarchical MgO and their application in water treatment. For example, Ai's group developed a sacrificial template-directed way to prepare mesoporous hierarchical MgO. The as-prepared MgO showed excellent removal capacities for Congo red.[8] Ng et al. reported template-free hydrothermal synthesis of mesoporous hierarchical MgO and their excellent ability of adsorbing the organic dye methyl orange.[20] Cao's group presented controllable biomimetic fabrication of MgO complex nanostructures with outstanding ability for dye.[18] In spite of these successes, the dye adsorption capacities of the reported MgO materials were not significantly higher than those reported on other adsorbents. In addition, most of existed synthesis methods required surfactants or hydrothermal/solvothermal process.

In this paper, we developed a facile and scaled-up route to synthesize porous hierarchical MgO based on an ethanol-assisted decomposition process, as a part of our continuous study on magnesium chemistry.[22−24] The as-synthesized porous hierarchical MgO exhibited superb adsorption performance for removing the Congo red dye from water. Congo red (1-naphthalene sulfonic acid, 3,30-(4,40-biphenylenebis(azo)) bis (4-amino-) disodium salt, $C_{32}H_{22}N_6O_6S_2Na_2$, CR), an azo anionic dye, is commonly used as a model pollutant to investigate the dye removal ability of adsorbents.[8−12,25−34] In this paper, the maximum adsorption capacity of CR on the as-obtained MgO reached above 2400 mg g^{-1}. To our knowledge, this value is the highest in all the reported data. The facile, cost-effective and scaled-up preparation process, and superhigh adsorption capacity for CR make the porous hierarchical MgO a promising candidate for practical applications.

2. EXPERIMENTAL SECTION

2.1. Preparation of Porous Hierarchical MgO. All reagents used during the process were analytical grade, unless otherwise noted. First, the aqueous $Mg(HCO_3)_2$ solution was prepared by bubbling CO_2 into 200 mL of an aqueous suspension of commercial light-burnt MgO (16 g L^{-1}) at the rate of 200 mL min^{-1} for 45 min. Then, the as-obtained $Mg(HCO_3)_2$ solution was added into vigorously stirred

Received: August 13, 2013
Accepted: November 13, 2013
Published: November 13, 2013

ethanol (100 mL, in a 500 mL three-necked flask) at 80 °C. After 5 min, the stirring was stopped and the solution was maintained at 80 °C for 2 h to form the $Mg_5(CO_3)_4(OH)_2{\cdot}4H_2O$ precursor. After that, the precursor was collected, filtered off, washed with water and ethanol three times, and dried in a blast drying oven at 60 °C for 4 h. Finally, the precursor was annealed in air at 400 °C for 4 h to obtain the porous hierarchical MgO.

2.2. Characterizations. The crystalline phases of the as-prepared samples were investigated by X-ray powder diffraction (XRD, Rigaku-DMax 2400) in reflection mode (Cu Kα radiation) at a scanning rate of 0.02 S^{-1} in the 2θ from 5 to 80°. The scanning electron microscope and transmission electron microscopy (SEM, JEOL-6360LV, operated at 20 kV; TEM, Philips TecnaiG2 20, operated at 200 kV) were performed to observe the shapes and structures of the as-obtained samples. The Fourier transform infrared (FTIR) spectra of the samples were measured on JASCO FT/IR-4100 spectrometric analyzer. The thermogravimetry analysis (TGA) of the precursor was carried out by a Mettler TG/SDTA851^e thermogravimetric analyzer at a heating rate of 10 °C min^{-1} in air. The N_2 adsorption−desorption isotherm was determined on a ASAP 2020 physisorption apparatus at the temperature of liquid nitrogen, in which the samples were degassed at 120 °C for 24 h before measurement. The surface area was calculated by the Brunauer−Emmett−Teller method.

2.3. Evaluation of Adsorption Performance. Congo red solutions with different concentrations (200, 500, 800, 1000, 1200, 1300, 1400 mg L^{-1}) were gained by dissolving CR with high purity water. Adsorption experiments were performed by mixing as-obtained porous hierarchical MgO with CR aqueous solution in a beaker (100 mL) under stirring at natural pH and room temperature. At different adsorption times, 5.0 mL of the mixture was collected and separated. The concentrations of CR in the filtrates were measured on Hitachi U-4100 UV−visible spectrophotometer.

The adsorption capacity of CR on the MgO sample was calculated by $q_t = (C_0 - C_t)V/m$, in which q_t is the adsorption capacity, C_0 and C_t are the concentrations of CR (mg L^{-1}) before and after adsorption, V is the volume of solution (L), and m is the mass of the MgO sample (g).

The effect of MgO dosage was performed by mixing a MgO sample of different weight to 80 mL of CR solution of 200 mg L^{-1} for 60 min. The weight of the MgO sample was adjusted to be in the range 0.008−0.04 g. To study kinetic, 0.04 g of the MgO sample was mixed with 80 mL of CR solution (200, 500, 1000, 1200 mg L^{-1}) for different times. The adsorption isotherms were finished by mixing MgO (0.04 g) to CR solutions (80 mL) of different initial concentrations for 60 min. The effect of pH was carried out by mixing MgO (0.04g) into a CR solution (80 mL) of 1000 mg L^{-1} with different pH (9.0, 11.0, 12.0, 13.0) for 60 min.

3. RESULT AND DISCUSSION

3.1. Synthesis of Porous Hierarchical MgO. Scheme 1 illustrates the synthesis process of the porous hierarchical MgO.

Scheme 1. Schematic Illustration of the Synthesis of Porous Hierarchical MgO

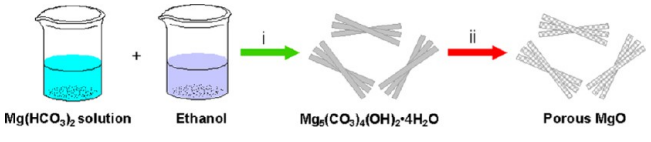

In the first step, the carbonate precursor could be directly obtained by decomposing $Mg(HCO_3)_2$ solutions at 80 °C in the presence of ethanol: ($5Mg(HCO_3)_2 \rightarrow Mg_5(CO_3)_4(OH)_2{\cdot}4H_2O + 6CO_2$). Xue's study has demonstrated that the $Mg_5(CO_3)_4(OH)_2{\cdot}4H_2O$ particles are easily self-assembled to form hierarchical structures.[35] The ethanol was used to accelerate reaction rate and control the morphology of magnesium carbonate. In the absence of ethanol, the magnesium carbonate particles were agglomerate and irregular (Figure S1, Supporting Information). This synthesis method is low-cost, environmentally benign, and quite easily scaled up to produce more than 1 kg of the product in one batch (Figure S2, Supporting Information). In the second step, the morphology-preserved MgO product was obtained by heat treating the $Mg_5(CO_3)_4(OH)_2{\cdot}4H_2O$ precursor ($Mg_5(CO_3)_4(OH)_2{\cdot}4H_2O \rightarrow 5MgO + 4CO_2 + 5H_2O$). Simultaneously, the thermal decomposition process was accompanied by the generation of large amounts of gases (e.g., CO_2 and H_2O), thus pores easily developed in the final annealed product.

To examine as-prepared magnesium carbonate precursor, the characterizations including X-ray powder diffraction (XRD), FTIR spectroscopy, Scanning electron microscopy (SEM), transmission electron microscopy (TEM), and thermogravimetric analysis (TGA) were carried out, as shown in Figures 1

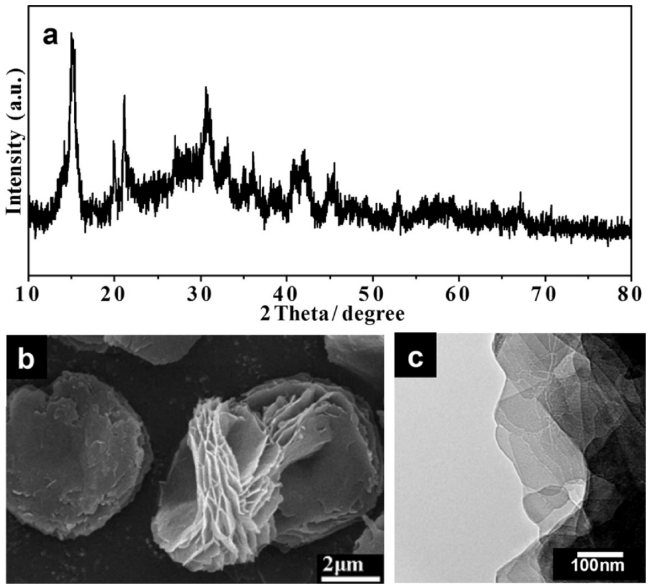

Figure 1. XRD pattern (a), SEM image (b), and TEM image (c) of carbonate precursor.

and S3 (Supporting Information). Figure 1a shows the XRD pattern of the carbonate precursor that can match well with $Mg_5(CO_3)_4(OH)_2{\cdot}4H_2O$ (JCPDS No. 25-0513). The wide diffraction peaks in the XRD pattern indicate the poor crystalline characteristic of the precursor. And no other impurity peak is detected, which suggests the precursor is pure. Figure S3a (Supporting Information) shows the FTIR spectrum of the carbonate precursor. The wide bands in 3600−3000 cm^{-1} were attributed to hydroxyl stretching, which came from H_2O in $Mg_5(CO_3)_4(OH)_2{\cdot}4H_2O$. The sharp band at 3650 cm^{-1} corresponded to the free OH. The bands at 1480 and 1420 cm^{-1} were assigned to vibrations of the carbonyl group (ν_3 mode). The three absorption bands at 800, 850, and 880 cm^{-1} were due to carbonate bending vibrations. Thus, it can be seen that the features in IR are consistent with $Mg_5(CO_3)_4(OH)_2{\cdot}4H_2O$. Figure S3b (Supporting Information) displays the typical SEM image of the carbonate precursor. It can be observed that the precursor is a hierarchical flowerlike particle with a diameter of 4−6 μm. The SEM image in Figure 1b reveals that the flowerlike particles are made up of a number of microsheets. Further structural information and

characterization of the carbonate precursor were obtained by TEM images in Figure 1c. The precursor particle is made up of a number of microsheets, which agrees well with the SEM observations. Figure S3c (Supporting Information) shows the typical TGA curve of the precursor. The TGA curve presented two significant weight loss steps: the first weight loss step occurred at 100−300 °C (DTG peaks at 241 °C) and was assigned to the loss of crystallized water and the decomposition of hydroxyl from $Mg_5(CO_3)_4(OH)_2{\cdot}4H_2O$; the second weight loss step occurred in range 350−500 °C (DTG peaks at 398 °C) and was attributed to the decomposition of the carbonate. The weight losses of two steps were about 26.3% and 37.4%, respectively. The theoretical values are 19.7% and 37.4%, respectively. This difference should be attributed to the existence of free water in the precursor. The TGA result reveals that the calcination temperature should be no less than 350 °C to obtain MgO.

Figures 2 and S4 (Supporting Information) show the typical XRD pattern, FTIR spectrum, and SEM images of the annealed

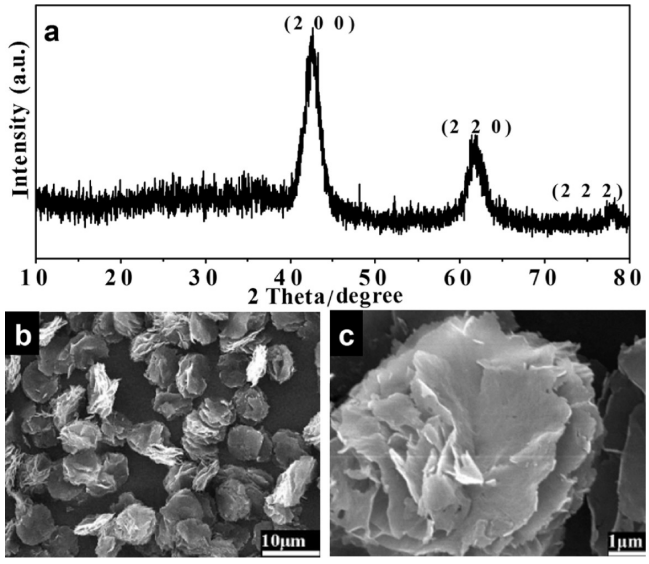

Figure 2. XRD pattern (a), SEM images (b, c) of MgO product.

product. As shown in Figure 2a, the XRD diffraction peaks can match well with the diffraction from the (200), (220), and (222) planes of MgO (JCPDS No. 45-0946), indicating that pure MgO can be obtained via the thermal decomposition of the $Mg_5(CO_3)_4(OH)_2{\cdot}4H_2O$ precursor at 400 °C. Moreover, the relatively broad diffraction peaks reveal that the MgO product should be in a small crystallite size. The grain size was determined to be 13.2 nm by Scherrer equation ($D = K\lambda/B \cos\theta$). The FTIR spectrum of the annealed product further confirms that the characteristic peaks assigned to the carbonate precursor completely disappeared after the thermal treatment. A new broad band around 400−800 cm^{-1} shown in Figure S4 (Supporting Information) was the characteristic of well-defined MgO. In addition, bands at about 3800−3100, 1610, and 1450 cm^{-1} were attributed to hydroxyl stretching, hydroxyl bending, and symmetric stretching of carbonate, respectively. It indicates that the surfaces of the MgO product can easily adsorb H_2O and CO_2 by chemistry when it is exposed to the atmosphere.

As shown in Figure 2b, the hierarchical flowerlike structures of the precursor were successfully preserved in the MgO product after calcination. The sizes of the flowerlike MgO particles were found to be 4−6μm, which is similar to that of the carbonate precursor. The SEM image in Figure 2c illustrates that the microstructure of the as-prepared MgO was not significantly different from those of the carbonate precursor (Figures 1b and S3b (Supporting Information)), except the existence of some cracks. As a result, it is reasonably expected that the pores would form in the MgO particles by generating gases (H_2O and CO_2) from the interior of the precursor during the thermal decomposition process.

To further examine the microstructure of the flowerlike MgO, TEM was performed (Figure 3). Figure 3a shows an

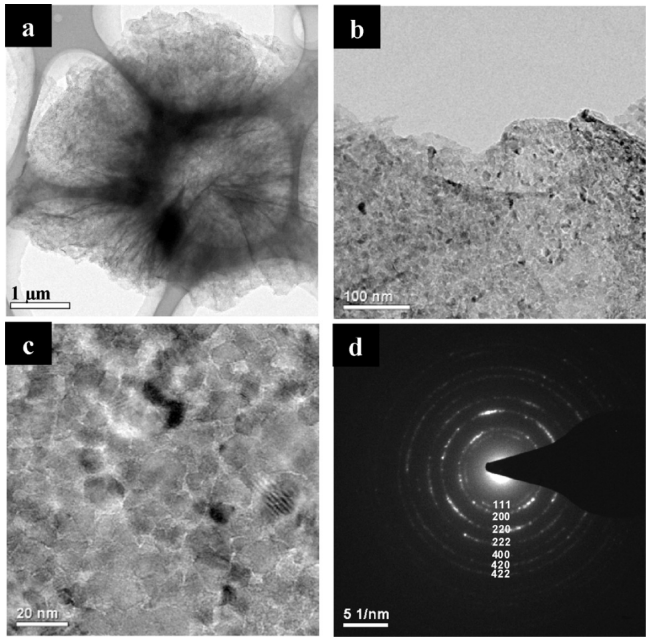

Figure 3. TEM (a, b, c) and SAED (d) images of the porous hierarchical MgO.

individual flowerlike MgO with a size of 5 μm, which agrees well with the SEM observations. The TEM image in Figure 3b reveals that the "petals" of flowerlike MgO are rather rough. That is significantly different from the carbonate precursor (Figure 1c). The magnified TEM image in Figure 3c shows that the petals are fabricated by numerous MgO nanoparticles with sizes of 10−15 nm. The selected area electron diffraction (SAED) of the product (Figure 3d) can match well with periclase (JCPDS No. 45-0946), which is consistent with the XRD results.

To analyze the porous structure of the as-obtained MgO, N_2 adsorption−desorption measurement was carried out. The N_2 adsorption/desorption isotherm (Figure 4) of the as-prepared MgO can not simply be assigned to any representative adsorption/desorption isotherms defined by IUPAC. At low relative pressure (P/P_0) range (0−0.05), the adsorption rapidly reaches saturation, suggesting the presence of micropores in the as-prepared MgO. At a higher relative pressure range (P/P_0 > 0.4), well-defined H-3 type hystereses are observed, indicating there exist disordered mesopores in the as-prepared MgO. Moreover, in isotherm curves, N_2 adsorption does not reach saturation, and the adsorption capacity increases rapidly at higher relative pressure (P/P_0 > 0.9), indicating the existence of macropores. Therefore, the isotherm curves display that micropores (<2 nm), mesopores (2−50 nm), and macropores

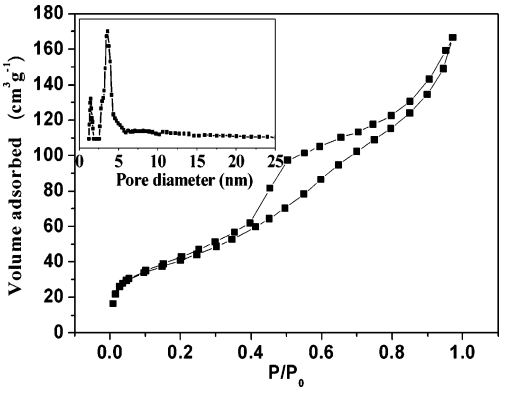

Figure 4. N_2 adsorption/desorption isotherms and pore-size distribution (inset) of the porous hierarchical MgO.

(>50 nm) coexist in the as-prepared MgO, suggesting the successful preparation of hierarchically porous structured MgO with micropores, mesopores, and macropores. The micropores and mesopores were created via an aforementioned gas release process during the thermal decomposition. And the macropores were made of flowerlike structures. The pore sizes exhibited bimodal distributions (inset in Figure 4), micropores with a peak diameter 1.3−1.7 nm and mesopores with peak diameter 2.7−4.5 nm, indicating hierarchical porous structure in the MgO. Moreover, Brunauer−Emmett−Teller (BET) specific surface area of as-prepared MgO was determined to be 148 m^2 g^{-1}. And the internal surface area and external surface areas were found to be 107 m^2 g^{-1} and 41 m^2g^{-1}, respectively. The specific surface area of MgO is very high. To illustrate this point, the reported specific surface area values of other reported MgO samples are listed in Table 1. As can be seen the specific surface area of the as-obtained MgO is similar with those of other reported MgO samples.

Table 1. Specific Surface Areas of Various MgO Samples

adsorbent	specific surface area (m^2 g^{-1})	references
porous hierarchical MgO	148	this paper
cubelike porous MgO	80	8
flowerlike MgO	72	19
mesoporous MgO	150	36
rodlike MgO	115	37
MgO nanoparticles	116	38
mesoporous MgO	151	39

3.2. Congo Red Adsorption Property. Generally, if the material has porous hierarchical structures and high surface area, it will possess more available active adsorption sites, efficient transport pathways, and may exhibit excellent adsorption performance. Herein, the as-synthesized porous hierarchical MgO was used to adsorb Congo red. Figure 5a shows the UV−vis absorption spectra of CR solutions after being treated by different dosages of the MgO with fixed initial concentration of 200 mg L^{-1}. With increase of MgO dosage, the removal efficiency of the CR increased. In particular, at a dosage of 0.50 g L^{-1}, the CR can be almost completely adsorbed, which was also supported by the color of the CR solution changing from deep red to colorless (in Figure 5b).

Figure 6 shows the time profile of Congo red adsorption at different initial concentrations with 0.50 g L^{-1} of the as-synthesized MgO. The adsorption rates were extraordinarily

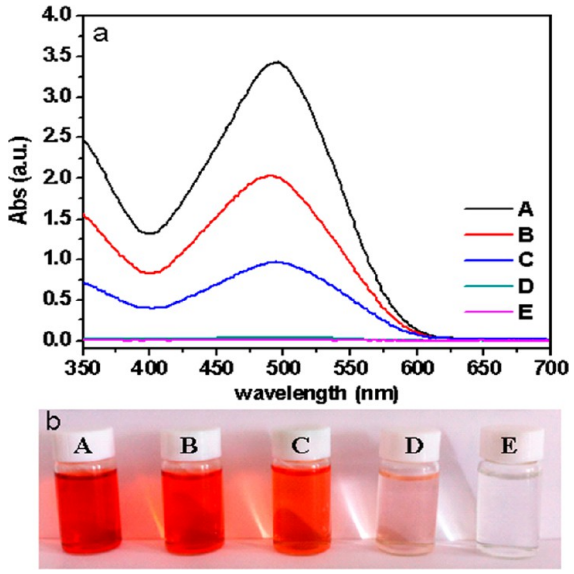

Figure 5. (a) UV−vis spectra of CR after being treated by the as-prepared MgO with different dosages: (A) 0 g L^{-1}, (B) 0.05 g L^{-1}, (C) 0.10 g L^{-1}, (D) 0.25 g L^{-1}, and (E) 0. 50 g L^{-1}. (b) Photo of initial CR (200 mg L^{-1}) aqueous solution treated by the MgO architectures with different dosages.

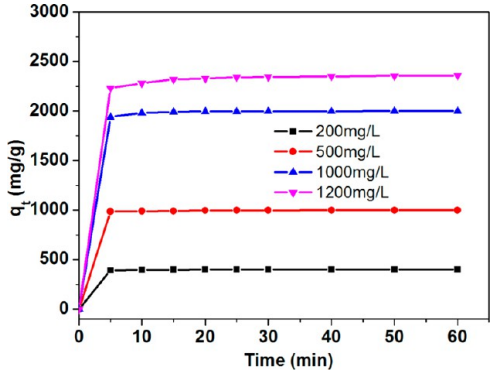

Figure 6. Time profiles of CR adsorption on the porous hierarchical MgO.

fast in the first 5 min under all concentrations. The adsorption nearly finished within 30 min, indicating the fast adsorption rate of CR on the MgO in water. It is noteworthy that the MgO exhibited an ultrahigh adsorption capacity of 2340 mg g^{-1} toward CR after 60 min of adsorption at the initial concentration of 1200 mg L^{-1} (Figures 6 and S5 (Supporting Information)). The porous hierarchical MgO is expected to become a promising material for rapid and deep treatment of high concentration dye-containing wastewater because of its features of fast adsorption rate and ultrahigh capacity.

The kinetics of CR removal on porous hierarchical MgO was further investigated. The pseudo-first-order kinetic models (eq 1) and pseudo-second-order kinetic models (eq 2) were applied to describe this adsorption process, respectively:

$$\log(q_e - q_t) = \log q_e - \frac{k_1 t}{2.303} \quad (1)$$

$$\frac{t}{q_t} = \frac{1}{k_2 q_e^{\,2}} + \frac{t}{q_e} \quad (2)$$

where q_e and q_t (mg g^{-1}) are the adsorption capacities at equilibrium and at any time t (min), respectively. k_1 (min^{-1}) and k_2 (g mg^{-1} min^{-1}) are the pseudo-first-order and pseudo-second-order rate constants, respectively. The kinetic parameters and the correlation coefficients (R^2) are given in Table S1 (Supporting Information). Figure 7 reveals that all the

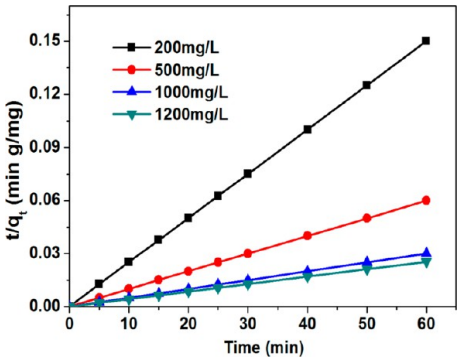

Figure 7. The pseudo-second-order kinetics plots of CR adsorption on the as-obtained MgO.

experimental data can fit well to the pseudo-second-order model with high correlation coefficients (R^2 > 0.999). The values of $q_{e,cal}$ were also very close to the values of $q_{e,exp}$, which indicates that the adsorption process of CR on the porous hierarchical MgO obeyed the pseudo-second-order model. The adsorption data also fit the pseudo-first-order model. However, the value of q_e was smaller than the value of q_t (Figure S6, Table S1, Supporting Information). This case is not logical, suggesting the inapplicability of the pseudo-first-order model to describe the adsorption of CR on the as-prepared MgO.

The effect of the initial concentration is shown in the adsorption isotherm (Figure S5, Supporting Information). It can be observed that when the initial concentrations are below 1200 mg L^{-1}, the adsorption capacity of CR on the as-obtained MgO linearly ascends with the increase of initial concentration; when the initial concentrations are above 1200 mg L^{-1}, with the increase of initial concentration, the adsorption capacity of CR on the as-obtained MgO slowly increase.

The relation between the adsorption capacity of CR on the as-obtained MgO and the equilibrium concentration of Congo red is shown in Figure 8. The Langmuir (eq 3) and Freundlich (eq 4) isotherms were used to describe this adsorption process, respectively.

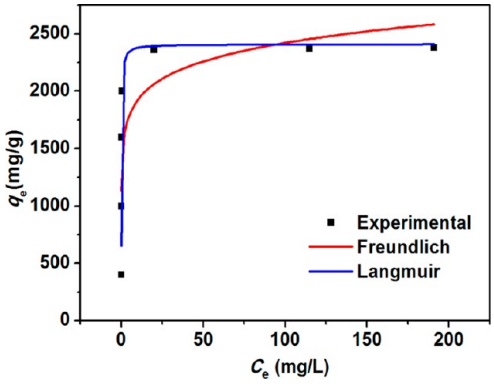

Figure 8. Adsorption isotherm curves of CR adsorption on the porous hierarchical MgO.

$$q_e = \frac{q_m b C_e}{1 + b C_e} \quad (3)$$

$$q_e = k_f C_e^{1/n} \quad (4)$$

in which q_m (mg g^{-1}) is the maximum adsorption capacity corresponding to complete monolayer coverage, b is the equilibrium constant (L·mg^{-1}), K_f is roughly an indicator of the adsorption capacity, and n is the adsorption intensity. The related parameters and the correlation coefficients (R^2) are listed in Table S2 (Supporting Information). The adsorption data were found to fit better to the Langmuir model with R^2 = 0.965, than to the Freundlich model with R^2 = 0.622, suggesting the monolayer adsorption.

The max adsorption capacity of Congo red on the as-synthesized MgO was found to be above 2409 mg g^{-1}. To our knowledge, this value is the highest in all the reported data, and is much higher than others. Up to now, many adsorbents have been used for removing CR and their adsorption capacities are normally below 500 mg g^{-1}, rarely above 1000 mg g^{-1}. Table 2 listed the removal capacities of porous hierarchical MgO and some typical adsorption materials reported previously.

Table 2. Adsorption Capacities of Congo Red on Various Adsorbents

adsorbent	removal capacity (mg g^{-1})	references
porous hierarchical MgO	2409	this paper
Fe_3O_4@meso C	1657	26
α-Fe/Fe_3O_4 composite	1297	34
porous MgO	689	8
hierarchical hollow NiO	440	32
hierarchical hollow FeOOH	275	12
activated carbon	~200	25
hierarchical hollow Fe_2O_3	160	33
functionalized carbon nanotubes	148	28
MgO nanoplates	131	29
Co_3O_4–Fe_3O_4 hollow spheres	125	30
commercial brucite	95	this paper
hierarchical Al_2O_3	90	11
jujuba seeds	56	31
clay materials	20	27

3.3. Analysis and Discussion. It is of deserved research to make it clear why hierarchical structured MgO has such a superb adsorption performance toward Congo red. According to the reported references, the adsorption of ionic dyes or organic pollutants may be associated with the electrostatic attraction and surface complexation.[4,40−43] First, the adsorption of Congo red on MgO can be attributed to electrostatic attraction. It is well known that if the pH of the solution is below the isoelectric point of adsorbent, the adsorbent will have positive surface charge and adsorb anionic dye molecules by electrostatic attraction. Congo red is a kind of anionic dye. The natural pH value (≈7.0) of the Congo red solution is much lower than the isoelectric point of MgO (12.1−12.7). Therefore, MgO can easily adsorb Congo red molecules at a natural pH. Besides electrostatic attraction, the adsorption of Congo red on MgO also may be associated with the other action. To investigate this point, the Congo red adsorption capacities of MgO were determined near the isoelectric point (pH = 11−13). In this case, the adsorption capacities were still above 1500 mg g^{-1} (Figure S7, Supporting Information), which

implies that Congo red can be adsorbed on the MgO even without electrostatic attraction.

To further investigate the adsorption mechanism, SEM, XRD, and IR of the CR-loaded adsorbent were carried out. The morphology of the CR-adsorbed MgO showed appreciable change: the microsheets of flowerlike particles turned to rough (Figure S8a, Supporting Information) with the formation of nanoflakes. The XRD patterns also exhibited significant changes, as shown in Figure S8b (Supporting Information): after adsorption, the MgO adsorbent changed into $Mg(OH)_2$ (JCPDS No. 07-0239). The FTIR spectrum in Figure 9a shows the peak intensity of CR-adsorbed adsorbent at 3650 cm^{-1} (free OH) increase, which indicates that adsorption process makes MgO change into $Mg(OH)_2$.

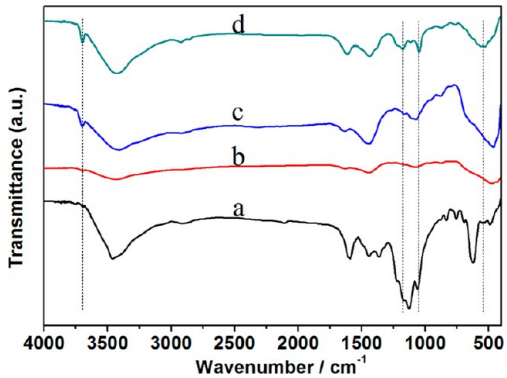

Figure 9. FTIR spectra of Congo red (a), hydrated MgO (at room temperature) (b), $Mg(OH)_2$ (c), and CR adsorbed adsorbent (d).

We know that the hydration degree of MgO is relatively low at room temperature, which can be observed in Figure 9b. Chen's group reported that the oxygen atom of the S═O group can be used as the hydrogen-bonding acceptor and form intramolecular hydrogen bonding with the oxygen-containing functional group of alkali-activated multiwalled carbon nanotubes.[4] Therefore, the formation of $Mg(OH)_2$ may be closely related to that S═O group of Congo red and can form intramolecular hydrogen bonding with the O group of MgO, as shown in Scheme 2. Moreover, FTIR spectra of CR adsorbed $Mg(OH)_2$ show new peaks at 1166.8, 1045.8, and 551.9 cm^{-1}, which suggests the surface complexation between CR and $Mg(OH)_2$.

On the basis of the above analysis, the adsorption mechanism of Congo red on MgO can be attributed to the electrostatic attraction and surface complexation. And the superb adsorption performance of MgO toward Congo red can be explained by this adsorption mechanism: when the isoelectric point of adsorbent is above the pH of CR solution, the adsorbent will have more surface positive charge and adsorb more anionic dye molecules, and vice versa. Both our work (Figure S7, Supporting Information) and the previous literature proved this point.[4,41] It is easy to understand that the MgO can more easily adsorb more CR molecules at a natural pH than the other adsorbents because of its high isoelectric point. The isoelectric points of common oxides are listed in the Table 3. It is clear

Scheme 2. Schematic Illustration of the Formation of Intramolecular Hydrogen Bonding

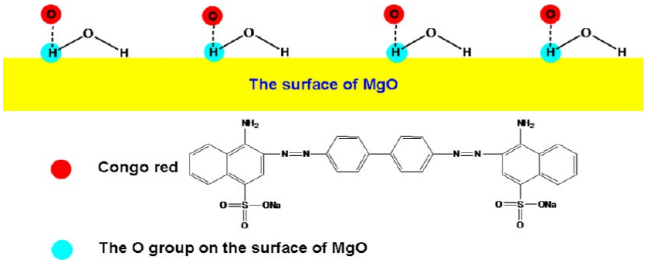

Table 3. The Isoelectric Points of Common Oxides[41,44]

oxide	isoelectric point
Sb_2O_5	<0.4
WO_3	<0.5
SiO_2	1–2
MnO_2	3.9–4.5
SnO_2	~5.5
TiO_2	~6
γ-Fe_2O_3	6.5–6.9
γ-Al_2O_3	7.0–9.0
α-Fe_2O_3	8.4–9.0
ZnO	8.7–9.7
NiO	~10.3
MgO	12.1–12.7

that the isoelectric point of MgO is the highest among the common oxides. Moreover, the Congo red removal capacity of porous hierarchical MgO near the isoelectric point is still much higher than that of the porous hierarchical NiO,[41] which indicates that the surface complexation between Congo red and MgO should be stronger than that between CR and other adsorbents.

According to the reported studies,[8,41] it can be speculated that such superior Congo red adsorption performance of the hierarchical porous MgO should be attributed not only to its high isoelectric point and strong surface complexation but also to its unique structure. To prove this point, MgO samples with different morphologies were synthesized and used to adsorb Congo red (as shown in Experimental Section and Figures S9–11, Supporting Information). Table S3 (Supporting Information) lists the Congo red adsorption capacities on hierarchical MgO, rodlike porous MgO, and cubelike porous MgO. It can be obviously observed that the adsorption performance of hierarchical MgO for CR is much better than those of rodlike porous MgO and cubelike porous MgO.

Hence, the superb adsorption performance of porous hierarchical MgO should be attributed to its high isoelectric point, strong surface complexation, and unique structures: the high isoelectric point and strong surface complexation make it so the MgO can easily adsorb negative Congo red molecules; the micropores and mesopores can provide a large number of active sites, whereas the coexisting macropores give short paths to enhance mass transfer and prevent blocking of the channels.

3.4. Recycling the Porous Hierarchical MgO. The regeneration performance of the adsorbent is an important factor in the actual application. During adsorption of Congo red, the molecular structure and microstructure of the porous hierarchical MgO adsorbent have changed, which means the recycling porous hierarchical MgO cannot be carried out by common routes, such as desorption[10] and catalytic oxidation.[24] To recycle the porous hierarchical MgO, we present a novel strategy, as shown in Scheme S1 (Supporting Information). This strategy includes three steps. (I) The adsorption of dye:

$MgO + H_2O$ + dye → dye loaded $Mg(OH)_2$; (II) Degradation and dissolution: dye loaded $Mg(OH)_2 + H_2O_2 + CO_2 + H_2O$ → $Mg(HCO_3)_2$ solution + mineralization product. (III) Regeneration: $Mg(HCO_3)_2$ → $Mg_5(CO_3)_4(OH)_2{\cdot}4H_2O$ → MgO. This work is under way and will be detailedly reported in our later article.

4. CONCLUSION

In summary, we have demonstrated a facile and scale-up method to prepare porous hierarchical MgO with enhanced Congo red adsorption performance. This method is quite easily scaled up to produce more than 1 kg of the sample. The as-prepared porous hierarchical MgO showed two advantageous structural features: a porous hierarchical structure and a high surface area, resulting in superb adsorption performance for Congo red (maximum adsorption capacity above 2400 mg g^{-1}). Such super adsorption performance of the porous hierarchical MgO can be attributed to its unique structures, high isoelectric point, and strong surface complexation. The adsorption process of the Congo red on porous hierarchical MgO was also systematically investigated, which was found to fit the pseudo-second-order rate equation and Langmuir adsorption model. The porous hierarchical MgO is expected to be a promising candidate for applications because of its facile, cost-effective and scaled-up preparation process, superb dye adsorption capacity, and regeneration performance.

■ ASSOCIATED CONTENT

Supporting Information

Preparation, SEM images, XRD patterns, N_2 adsorption−desorption curves, and adsorption performance of the MgO samples with different morphology (Experiment, Figures S9, S10, S11, and Table S3), SEM image of the magnesium carbonate obtained without ethanol (Figure S1), photos of pilot-scale equipment and product (Figure S2), characterizations of carbonate precursor (Figure S3), FTIR spectrum of the MgO sample (Figure S4), adsorption isotherms of Congo red on the hierarchical flowerlike MgO (Figure S5), the pseudo-first-order kinetics plots of Congo red adsorption (Figure S6), the adsorption parameter of kinetics for the adsorption of Congo red on MgO (Table S1), adsorption parameter of isotherm for the adsorption of Congo red on MgO (Table S2), the effects of pH on the adsorption capacity of CR onto MgO (Figure S7), SEM images and XRD pattern of the CR adsorbed adsorbent (Figure S8), and schematic illustration of recycling the porous hierarchical MgO (Scheme S1). This material is available free of charge via the Internet at http://pubs.acs.org.

■ AUTHOR INFORMATION

Corresponding Author

*G.-l. Ning. E-mail: ninggl@dlut.edu.cn. Fax/Tel: (+86)411-84986065.

Notes

The authors declare no competing financial interest.

■ ACKNOWLEDGMENTS

This work was supported by National Natural Science Foundation of China (21076041 and 21276046), the Fundamental Research Funds for the Central Universities of China (DUT13RC(3)43), the Ministry of Education Science and technology research projects, and High-Tech R & D projects in the magnesium industry of the Liaoning Province, China.

■ REFERENCES

(1) Grégorio, C. *Bioresour. Technol.* **2006**, *97*, 1061−1085.
(2) Jain, R.; Sikarwar, S. *Int. J. Environ. Pollut.* **2006**, *27*, 158−178.
(3) Liu, F.; Chung, S. Y.; Oh, G.; Seo, T. S. *ACS Appl. Mater. Interfaces* **2012**, *4*, 922−927.
(4) Ma, J.; Yu, F.; Zhou, L.; Jin, L.; Yang, M. X.; Luan, J .S.; Tang, Y. H.; Fan, H. B.; Yuan, Z. W.; Chen, J. H. *ACS Appl. Mater. Interfaces* **2012**, *4*, 5749−5760.
(5) Miao, Y. E.; Wang, R. Y.; Chen, D.; Liu, Z. Y.; Liu, T. X. *ACS Appl. Mater. Interfaces* **2012**, *4*, 5353−5359.
(6) Nikolina, A. T.; George, Z. K.; Nikolaos, K. L.; Eleni, A. D. *Langmuir* **2013**, *29*, 1657−1668.
(7) Hu, J. S.; Zhong, L. S.; Song, W. G.; Wan, L. J. *Adv. Mater.* **2008**, *20*, 2977−2982.
(8) Ai, L. H.; Yue, H. T.; Jiang, J. *Nanoscale* **2012**, *4*, 5401−5408.
(9) Fei, J. B.; Cui, Y.; Yan, X. H.; Qi, W.; Yang, Y.; Wang, K. W.; He, Q.; Li, J. B. *Adv. Mater.* **2008**, *20*, 452−456.
(10) Fei, J. B.; Cui, Y.; Zhao, J.; Gao, L.; Yang, Y.; Li, J. B. *J. Mater. Chem.* **2011**, *21*, 11742−11746.
(11) Cai, W. Q.; Yu, J. G.; Jaroniec, M. *J. Mater. Chem.* **2010**, *20*, 4587−4594.
(12) Wang, B.; Wu, H. B.; Yu, L.; Xu, R.; Lim, T. T.; Lou, X. W. *Adv. Mater.* **2012**, *24*, 1111−1116.
(13) Xiao, H. Y.; Ai, Z. H.; Zhang, Z. L. *J. Phys. Chem. C* **2009**, *113*, 16625−16630.
(14) Yu, X. Y.; Xu, R. X.; Gao, C.; Luo, T.; Jia, Y.; Liu, J. H.; Huang, X. J. *ACS Appl. Mater. Interfaces* **2012**, *4*, 1954−1962.
(15) Mou, F. Z.; Guan, J. G.; Ma, H. R.; Xu, L. L.; Shi, W. D. *ACS Appl. Mater. Interfaces* **2012**, *4*, 3987−3993.
(16) Bain, S. W.; Ma, Z.; Cui, Z. M.; Zhang, L. S.; Niu, F.; Song, W. G. *J. Phys. Chem. C* **2008**, *112*, 11340−11344.
(17) Liu, W. Z.; Huang, F.; Wang, Y. J.; Zou, T.; Zheng, J. S.; Lin, Z. *Environ. Sci. Technol.* **2011**, *45*, 1955−1961.
(18) Wu, X. M.; Cao, H. Q.; Yin, G.; Yin, J. F.; Lu, Y. X.; Li, B. *J. Phys. Chem. Chem. Phys.* **2011**, *13*, 5047−5052.
(19) Cao, C. Y.; Qu, J.; Wei, F.; Liu, H.; Song, W. G. *ACS Appl. Mater. Interfaces* **2012**, *4*, 4283−4287.
(20) Lian, J. B.; Zhang, C. H.; Wang, P.; Ng, D. H. L. *Chem.−Asian J.* **2012**, *7*, 2650−2655.
(21) Nguyen, K. N.; Phi, T. T. H.; Tran, D. L.; Tran, Q. H. *J. Colloid Interface Sci.* **2013**, *398*, 210−216.
(22) Tian, P.; Ye, J. W.; Xu, N.; Gong, W. T.; Zhang, Q. S.; Lin, Y.; Ning, G. L. *Chem. Commun.* **2011**, *47*, 12008−12010.
(23) Pang, H. C.; Ning, G. L.; Gong, W. T.; Ye, J. W.; Lin, Y. *Chem. Commun.* **2011**, *47*, 6317−6319.
(24) Tian, P.; Ye, J. W.; Ning, G. L.; Gong, W. T.; Xu, N.; Zhang, Q. S.; Lin, Y. *RSC. Adv.* **2012**, *2*, 10217−10221.
(25) Purkait, M. K.; Maiti, A.; DasGupta, S.; De, S. *J. Hazard. Mater.* **2007**, *145*, 287−295.
(26) Huang, J.; Chen, W. M.; Zhao, W.; Li, Y. Q.; Li, X. G.; Chen, C. P. *J. Phys. Chem. C* **2009**, *113*, 12067−12071.
(27) Vimonses, V.; Lei, S. M.; Jin, B.; Chowd, C. W. K.; Saint, C. *Chem. Eng. J.* **2009**, *148*, 354−364.
(28) Mishra, A. K.; Arockiadoss, T.; Ramaprabhu, S. *Chem. Eng. J.* **2010**, *162*, 1026−1034.
(29) Hu, J. C.; Song, Z.; Chen, L. F.; Yang, H. J.; Li, J. L.; Richards, R. *J. Chem. Eng. Data* **2010**, *55*, 3742−3748.
(30) Wang, X.; Zhong, Y. T.; Zhai, T. Y.; Guo, Y. F.; Chen, S. M.; Ma, Y.; Yao, J. N.; Bando, Y.; Golberg, D. *J. Mater. Chem.* **2011**, *21*, 17680−17687.
(31) Reddy, M. C. S.; Sivaramakrishna, L.; Reddy, A. V. *J. Hazard. Mater.* **2012**, *203-204*, 118−127.
(32) Zhu, T.; Chen, J. S.; Lou, X. W. *J. Phys. Chem. C* **2012**, *116*, 6873−6878.
(33) Wei, Z. H.; Xing, R. G.; Zhang, X.; Liu, S.; Yu, H. H.; Li, P. C. *ACS Appl. Mater. Interfaces* **2013**, *5*, 598−604.

(34) Wang, L. X.; Li, J. C.; Wang, Z. T.; Zhao, L. J.; Jiang, Q. *Dalton Trans.* **2013**, *42*, 2572−2579.
(35) Yan, C.L.; Xue, D. F. *J. Phys. Chem. B* **2005**, *109*, 12358−12361.
(36) Li, W. C.; Lu, A. H.; Weidenthaler, C.; Schuth, F. *Chem. Mater.* **2004**, *16*, 5676−5681.
(37) Sutradhar, N.; Sinhamahapatra, A.; Pahari, S. K.; Pal, P.; Bajaj, H. C.; Mukhopadhyay, I.; Panda, A. B. *J. Phys. Chem. C* **2011**, *115*, 12308−12316.
(38) Ruminski, A. M.; Jeon, K. J.; Urban, J. J. *J. Mater. Chem.* **2011**, *21*, 11486−11491.
(39) Eckhardt, B.; Ortel, E.; Polte, J.; Bernsmeier, D.; Görke, O.; Strasser, P.; Kraehnert, R. *Adv. Mater.* **2012**, *24*, 3115−3119.
(40) Cai, W. Q.; Yu, J. G.; Cheng, B.; Su, B. L.; Jaroniec, M. *J. Phys. Chem. C* **2009**, *113*, 14739−14746.
(41) Cheng, B.; Le, Y.; Cai, W. Q.; Yu, J. G. *J. Hazard. Mater.* **2011**, *185*, 889−897.
(42) Yu, F.; Ma, J.; Wu, Y. Q. *J. Hazard. Mater.* **2011**, *192*, 137−1379.
(43) Yu, F.; Wu, Y. Q.; Ma, J. *J. Hazard. Mater.* **2012**, *237*−*238*, 102−109.
(44) Parks, G. A. *Chem. Rev.* **1965**, *65*, 177−198.